

# Microstructural Origins of Energy Storage During Plastic Deformation of 310S TWIP Steel

Sandra Musiał<sup>a,\*</sup>, Michał Maj<sup>a</sup>, Marcin Nowak<sup>a</sup>

<sup>a</sup>*Institute of Fundamental Technological Research, Polish Academy of Sciences,  
Pawińskiego 5B, 02-106 Warsaw, Poland*

---

## Abstract

The microstructural mechanisms governing energy storage during plastic deformation of twinning-induced plasticity (TWIP) steels remain insufficiently understood, particularly under conditions of strain localization. This study provides a crystallographic-scale interpretation of energy storage in 310S TWIP steel exhibiting complex deformation mechanisms.

Electron backscatter diffraction (EBSD) was used to characterize the evolution of local crystallographic orientation and microtexture during uniaxial tensile deformation using two complementary approaches: tracking the same surface region at successive strain levels and analysing regions corresponding to known local plastic strain. Deformation was initially dominated by dislocation slip, while twinning activity increased significantly beyond an equivalent plastic strain of  $\bar{\epsilon}^p \approx 0.3$ . Progressive deformation produced pronounced lattice rotations and the development of a dual-fibre texture consisting of a dominant  $\langle 111 \rangle \parallel \text{RD}$  component and a secondary  $\langle 100 \rangle \parallel \text{RD}$  component associated with deformation twinning.

Correlation with previously quantified energy storage behaviour obtained from coupled digital image correlation and infrared thermography measurements reveals that intensified twinning and texture evolution in strain-localized regions are accompanied by a marked reduction in the energy storage rate. The results indicate that twin-matrix refinement and lattice rotation progressively reduce the material's capacity to store deformation energy and create favourable conditions for shear-band-mediated deformation.

*Keywords:* TWIP steel, EBSD, plastic deformation, texture evolution, energy storage

---

---

\*Corresponding author: smusial@ippt.pan.pl

# 1. Introduction

Transformation-induced plasticity (TRIP) and twinning-induced plasticity (TWIP) phenomena have been extensively studied in high-alloy austenitic steels because they enable an exceptional combination of strength, ductility, and energy absorption during plastic deformation. These properties arise from deformation mechanisms beyond conventional dislocation slip. In TRIP steels, plastic deformation promotes martensitic transformation, whereas TWIP steels accommodate strain primarily through mechanical twinning. Both mechanisms sustain strain hardening, delay necking, and improve fracture resistance, making these alloys attractive for structural and energy-absorbing applications [1, 2, 3, 4].

The stacking fault energy (SFE) is widely recognized as the primary parameter governing deformation mechanisms in face-centred cubic (FCC) alloys. Deformation twinning typically occurs for SFE values in the range of 20 – 50 mJ/m<sup>2</sup>, whereas martensitic transformation becomes dominant below approximately 15 – 20 mJ/m<sup>2</sup> [1]. Alloys with intermediate SFE exhibit complex deformation behaviour involving dislocation slip, stacking faults, twinning, and, in some cases, martensitic transformation, which strongly influences strain hardening and microstructural evolution [2, 5]. In addition to chemical composition [6, 7], deformation mechanisms in TWIP/TRIP steels are affected by temperature [8], strain rate [9], grain size, and crystallographic orientation [3, 10, 11]. Twinning activity depends strongly on grain orientation and Schmid factor distribution, while temperature-induced changes in SFE can shift the dominant deformation mode either from phase transformation to twinning [12] or from twinning to slip [8]. Recent work has also highlighted the importance of unstable fault energies (USFE and UTFE) as indicators of deformation-mode selection [13]. Together, these studies demonstrate that TWIP steels exhibit strongly coupled microstructural and mechanical responses during deformation.

At large plastic strains, deformation texture evolution in FCC materials is strongly influenced by mechanisms producing intense lattice rotation, including strain localization and shear-band-mediated deformation. In low- and intermediate-SFE alloys, localized shear accommodates plastic incompatibility between deformation substructures and promotes crystallographic reorientation beyond that produced by slip and twinning alone. Texture transitions involving Copper, Brass, and Goss components have been linked to shear-band-associated lattice rotation at advanced deformation levels [14, 15, 16]. These mechanisms are particularly relevant in TWIP steels, where deformation twinning interacts with lattice rotation during strain localization.

Alongside microstructural evolution, plastic deformation involves conversion of mechanical work into stored energy and heat. Energy storage reflects the formation and interaction of lattice defects during deformation [17]. Since the classical work of Taylor and Quinney [18], it has been recognized that the fraction of stored energy evolves during deformation [19, 20, 21, 22]. To describe instantaneous energy conversion, the energy storage rate

$$Z = \frac{de_s}{dw_p}. \quad (1)$$

was introduced [23]. The evolution of  $Z$  reflects changes in active deformation mechanisms and defect structures. Experimental investigation of energy conversion during plastic deformation has been enabled by combined Digital Image Correlation (DIC) and Infrared Thermography (IRT), which allow investigation of local thermomechanical behaviour [24], for example during Lüders band propagation [25, 26] and reconstruction of plastic work and heat sources [27, 28, 29]. In particular, the energy balance during tensile deformation of 310S austenitic steel was quantified in [30], where the evolution of plastic work, dissipated heat, and energy storage rate was determined experimentally, accounting for both thermoelastic effect and heat exchange with the surroundings.

Energy storage has also been examined from complementary microstructural perspectives. In [31] plastic instability was analysed using thermomechanical measurements combined with transmission electron microscopy (TEM), relating stored energy to defect structures observed at the microscale. More generally, energy storage during plastic deformation governed primarily by dislocation slip is often interpreted using the concept of low-energy dislocation structures (LEDSs) [32, 33, 34], in which continued deformation promotes rearrangement of dislocations into configurations of reduced energy. Such approaches relate stored energy mainly to dislocation density and organization. However, in materials where deformation twinning contributes significantly to plasticity, crystallographic reorientation and texture evolution may also influence stored energy, particularly under conditions of localized plastic deformation. This relationship remains insufficiently clarified in TWIP-deforming austenitic steels.

The present work addresses this gap by correlating electron backscatter diffraction (EBSD) - based characterization of microtexture evolution with previously determined energy-storage measurements for 310S TWIP steel. The analysis focuses on the stage of strain localization, where twin-matrix refinement and pronounced lattice rotation occur. Although the macroscopic energy balance during tensile deformation of 310S steel was previously quantified in [30], that work focused on thermomechanical measurements and evaluation of energy conver-

sion parameters. The present study constitutes an independent microstructural investigation that uses those energetic results as a reference framework. By correlating EBSD observations with macroscopic energy-storage behaviour, this work provides a microstructural interpretation of energy storage mechanisms in TWIP-deforming austenitic steel.

## 2. Material and methods

The investigated material was 310S austenitic stainless steel, which is widely used in high-temperature applications due to its excellent oxidation resistance and mechanical stability. It is considered a candidate structural material for supercritical water-cooled reactors (SCWRs), where long-term exposure to aggressive environments imposes stringent requirements on microstructural stability [7]. The chemical composition of the material is listed in Table 1.

Table 1: Chemical composition of tested material (in wt%).

	C	S	P	Mn	Si	Cr	Ni	N	Fe
310S	0.08	0.015	0.045	2.0	0.75	24.0–26.0	19.0–22.0	0.11	balance

Owing to its high nickel content, the austenitic phase remains stable during plastic deformation and no deformation-induced martensitic transformation is expected. The SFE, estimated using the empirical relation proposed in [6], lies in the range of 35.3 – 43.4 mJ/m<sup>2</sup>. Accordingly, plastic deformation is governed primarily by deformation twinning accompanied by dislocation slip, characteristic of TWIP steels.

Specimens for thermomechanical testing and microstructural characterization were extracted from a cold-rolled sheet after annealing at 1373 K followed by air/water spray quenching. The initial microstructure was characterized by EBSD using a Zeiss Crossbeam 350 scanning electron microscope equipped with an EDAX Hikari detector. Figure 1 presents the inverse pole figure (IPF) map acquired in the RD–TD plane and transformed into the TD–ND plane, together with the corresponding (111) pole figure (RD, TD, and ND denote the rolling, transverse, and normal directions, respectively). The material exhibits a fully austenitic microstructure with equiaxed grains and an average grain size of approximately 21  $\mu\text{m}$ . A high density of annealing twins is observed, predominantly with straight and parallel morphology, while the initial crystallographic texture is weak.

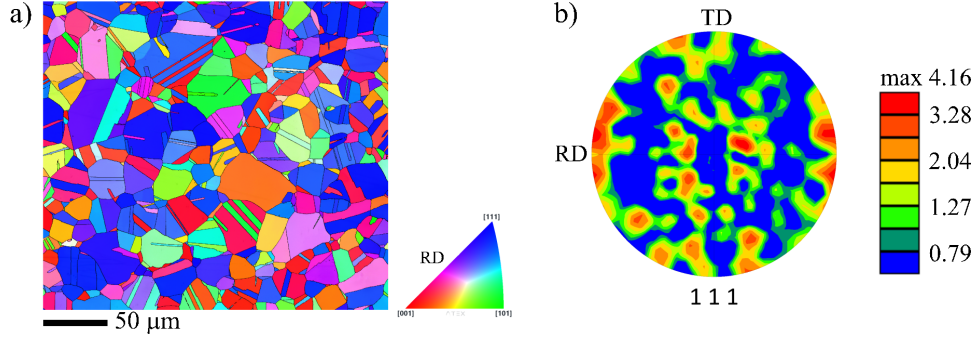


Figure 1: (a) IPF map representing grain orientations with respect to RD and (b) corresponding (111) pole figure of 310S steel in the reference state.

Microstructural evolution during deformation was investigated using two complementary EBSD-based approaches. In the first approach, the evolution of crystallographic orientations within the same surface region was tracked at successive stages of deformation. The specimen surface was initially electropolished, and a rectangular region of interest was defined by marking its vertices using focused ion beam (FIB) milling. An EBSD map of this region was acquired in the undeformed state. The specimen was then subjected to uniaxial tensile loading with intermediate unloading steps, and EBSD measurements of the same region were performed after each loading-unloading cycle (Fig. 2). This approach enabled direct tracking of orientation changes relative to the initial state. However, progressive surface roughening during deformation, combined with the near-surface nature of EBSD measurements, limited the accuracy of point-to-point spatial correspondence at higher strains.

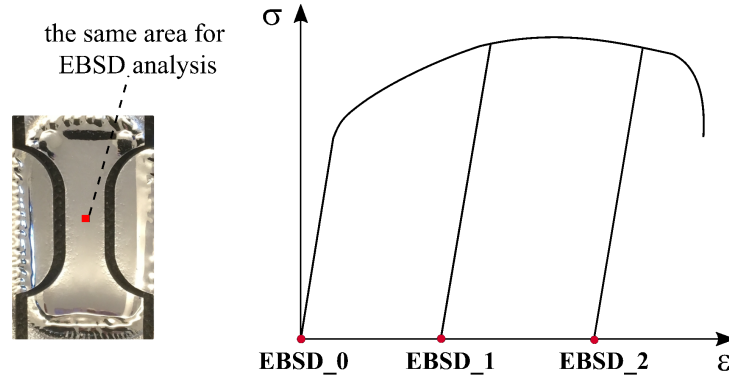


Figure 2: Tracking of crystallographic orientation in the same area during deformation: (left) analysed region in the reference state; (right) schematic of sequential loading with intermediate unloadings and EBSD measurements.

In the second approach, EBSD maps were acquired from different regions corresponding to known local strain levels. Specimens were deformed in uniaxial tension up to just prior to

fracture (Fig. 3). The surface distribution of equivalent plastic strain was determined using DIC supported by a calibrated mechanical model. Based on this distribution, regions representing different strain levels were selected for EBSD analysis. To assess through-thickness homogeneity, specimens were sequentially electropolished to depths corresponding to one-quarter, one-half, and three-quarters of the sheet thickness, and EBSD measurements were performed on the resulting longitudinal cross-sections. This ensured that the analysed regions represented bulk material and provided improved surface quality and spatial resolution. This approach enabled analysis of texture evolution as a function of strain, although direct comparison with the initial state was not possible.

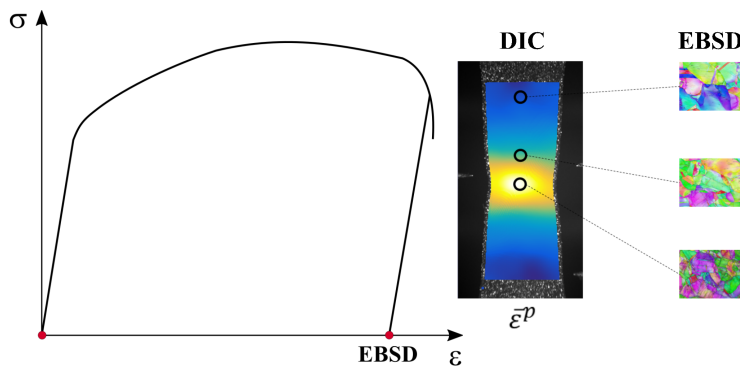


Figure 3: EBSD analysis of regions with different strain levels: (left) schematic of tensile test interrupted before fracture; (right) distribution of equivalent plastic strain with selected regions for EBSD measurements.

EBSD measurements were performed at an accelerating voltage of 25 kV in high-current mode using a 60  $\mu\text{m}$  aperture. Step sizes of 200, 100, and 50 nm were selected depending on the required spatial resolution. Data processing and visualization were carried out using ATEX software [35] and EDAX OIM Analysis. All EBSD orientation maps were primarily acquired on the RD-TD surface and subsequently transformed into the TD-ND reference frame to enable direct interpretation with respect to the tensile axis ( $\parallel\text{RD}$ ). In addition, a complementary map was obtained directly in the RD-ND plane at an advanced stage of deformation within the necking region, providing insight into characteristic microstructural features from a through-thickness perspective.

### 3. Results and discussion

#### 3.1. Macroscopically determined energy conversion

The results presented in this section are based on displacement and temperature fields measured during uniaxial tensile tests and analysed using the thermomechanical framework proposed in [30].

Using this methodology, surface distributions of plastic work  $w_p$  and energy dissipated  $q_d$  were obtained, enabling evaluation of energy storage rate  $Z$  at selected material points. The present study focuses on the dataset corresponding to a strain rate of  $\dot{\epsilon} = 1/s$  and additionally presents, for the first time, the surface distribution of  $Z$ .

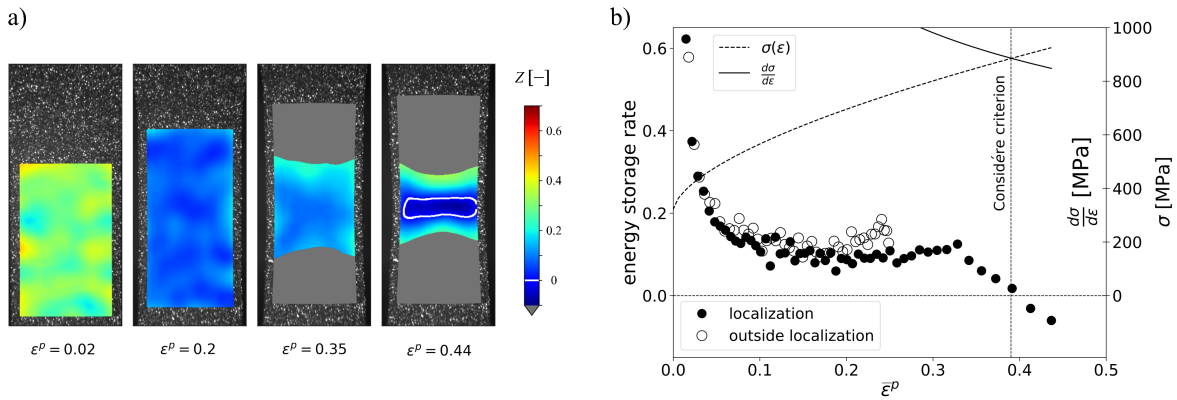


Figure 4: (a) Surface distributions of energy storage rate  $Z$  at selected stages of deformation and (b) evolution of  $Z$  at representative points located within and outside the localization zone [30], with the point corresponding to the Considère criterion indicated on the stress–strain curve.

Figure 4a shows the surface distributions of  $Z$  at different stages of deformation, while Fig. 4b presents the evolution of  $Z$  at two representative points: one located within the localization zone and the other outside it. In addition, Fig. 4b indicates the point on the stress–strain curve at which the Considère criterion is satisfied.

At average plastic strains of  $\epsilon^p = 0.02$  and  $\epsilon^p = 0.2$ , the  $Z$  field remains spatially uniform, and the evolution of  $Z$  at both points is similar, indicating macroscopically homogeneous deformation. At  $\epsilon^p = 0.02$ , relatively high values of  $Z$  (on the order of 0.4) are observed. With increasing plastic strain,  $Z$  decreases, reaching approximately 0.1–0.15 at  $\epsilon^p = 0.2$ . The distributions corresponding to  $\epsilon^p = 0.35$  and  $\epsilon^p = 0.44$  represent stages of strain localization. In these cases,  $Z$  is evaluated only within the localized deformation zone, while regions outside - where plastic flow has ceased - are shown in grey. Accordingly, the evolution of

$Z$  at the point outside the localization zone is plotted only up to the onset of localization. In the final stage, immediately prior to fracture,  $Z$  decreases rapidly and reaches negative values, indicating that the material locally loses its ability to store energy before failure. The boundary of the region where the energy storage rate becomes non-positive ( $Z \leq 0$ ) is marked by a white contour. A negative value of  $Z$  implies that, for a given increment of plastic strain, the energy dissipated as heat exceeds the plastic work, which can occur only if part of the energy stored during earlier stages of deformation is released. It is observed that the  $Z = 0$  condition is reached at a plastic strain similar to that corresponding to the Considère criterion.

### 3.2. Microstructure evolution

Figure 5 presents inverse pole figure (IPF) maps of the same region at successive stages of deformation: the initial state (Fig. 5a), macroscopically uniform deformation (Fig. 5b), and the stage of plastic strain localization (Fig. 5c). The maps are colour-coded with respect to the rolling direction (RD). EBSD analysis was performed with a step size of 100 nm.

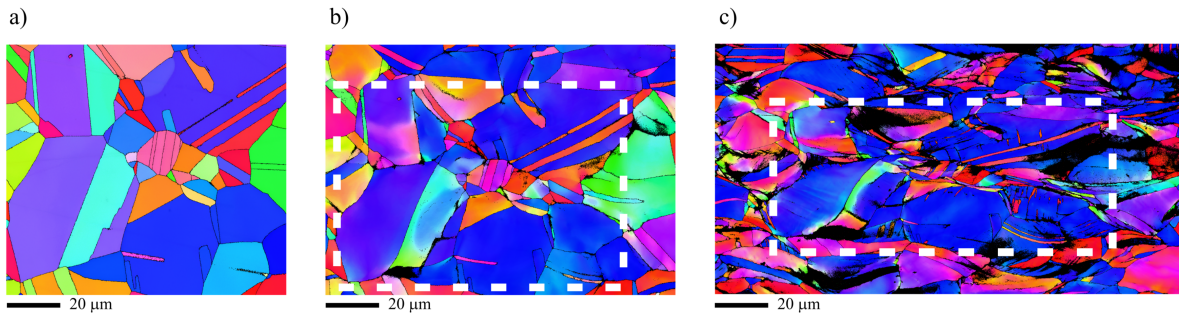


Figure 5: Orientation maps of the same area: (a) initial state, (b) macroscopically uniform deformation, (c) strain localization. The analysed region is marked by a white dashed line in (b) and (c).

Based on this sequence, the evolution of individual grain orientations was analysed. Figure 6 shows grain reference orientation deviation (GROD) distributions for two representative grains (A and B) with different initial orientations. GROD quantifies the local misorientation relative to the average grain orientation in the undeformed state. The maps correspond to macroscopically uniform deformation and strain localization.

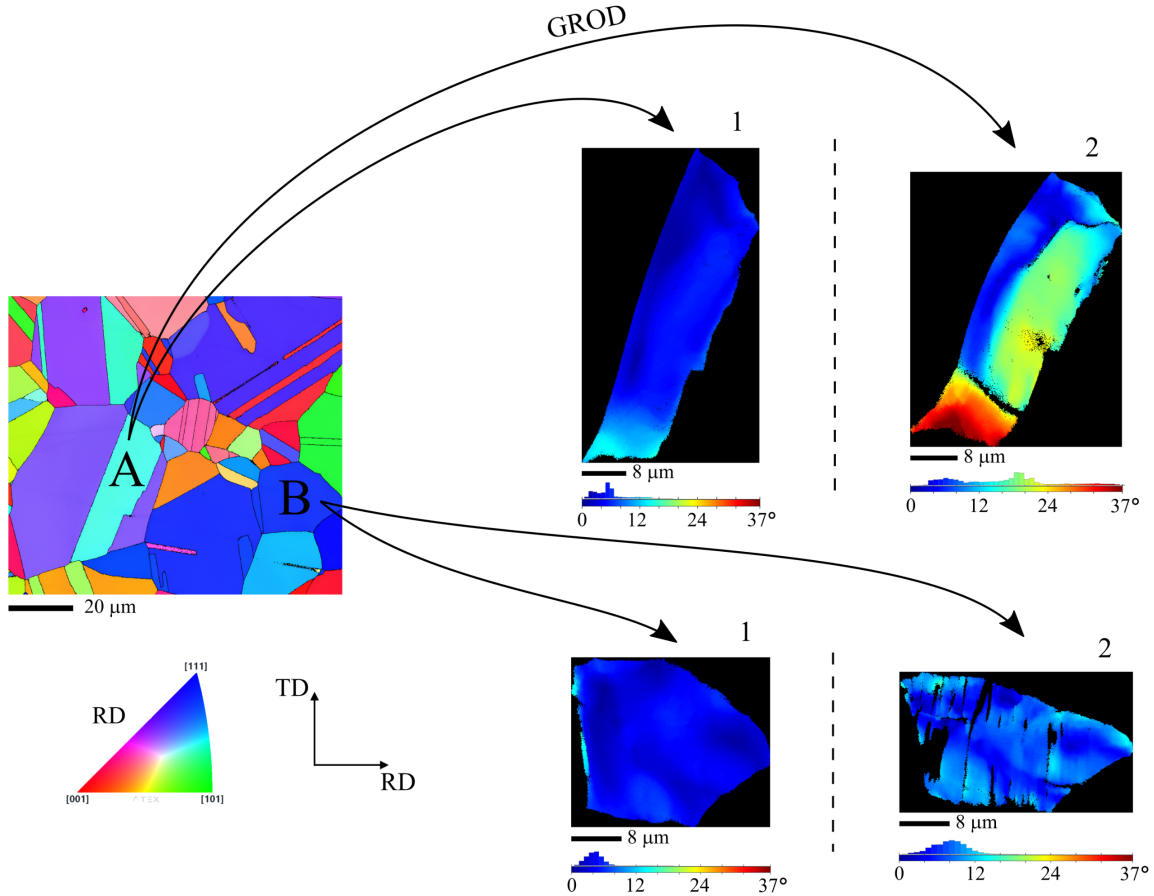


Figure 6: GROD distributions in grains A and B for (1) macroscopically uniform deformation and (2) strain localization.

Grain A exhibits significantly higher GROD values than grain B, particularly at the stage of localized deformation. In grain A, GROD reaches up to  $37^\circ$ , with three distinct subregions emerging; their boundaries become more pronounced during localization. In contrast, grain B shows a maximum GROD of  $15^\circ$ , with less pronounced internal heterogeneity.

These differences arise from the distinct initial crystallographic orientations of the grains, which influence the preferred deformation mechanisms. This tendency was evaluated using Schmid's law, applied to both slip and twinning systems [36]. Figure 7 shows the corresponding Schmid factor distributions for  $\{111\}\langle 110 \rangle$  slip ( $SF^{slip}$ ) and  $\{111\}\langle 112 \rangle$  twinning ( $SF^{twin}$ ) systems in the initial state.

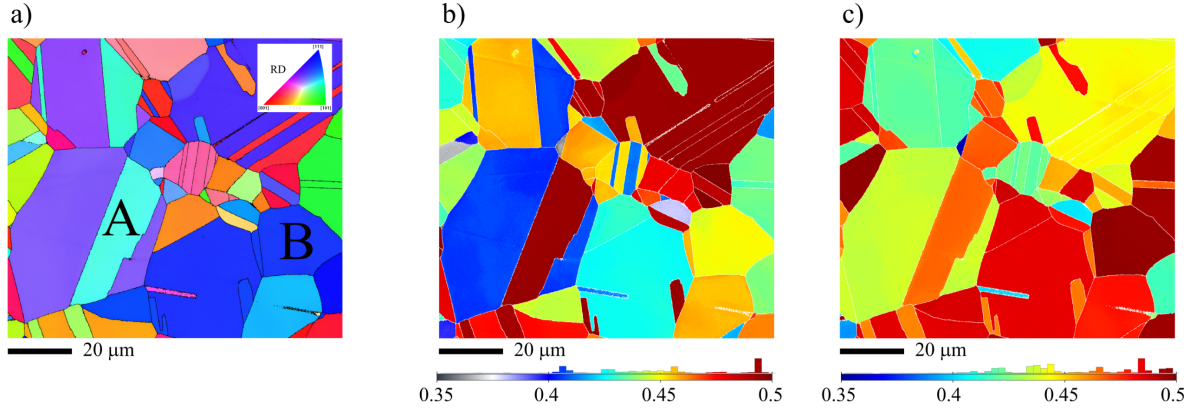


Figure 7: (a) Initial orientation map; (b) Schmid factor for slip ( $SF^{slip}$ ); (c) Schmid factor for twinning ( $SF^{twin}$ ).

The Schmid factors were calculated considering 24 slip systems and 12 forward twinning systems. Grain A exhibits  $SF^{slip} = 0.495$  and  $SF^{twin} = 0.466$ , indicating a preference for dislocation slip, whereas grain B ( $SF^{slip} = 0.45$ ,  $SF^{twin} = 0.497$ ) is more favourably oriented for twinning. Figure 8 presents disorientation profiles for grains A and B at the stages of macroscopically uniform deformation and strain localization.

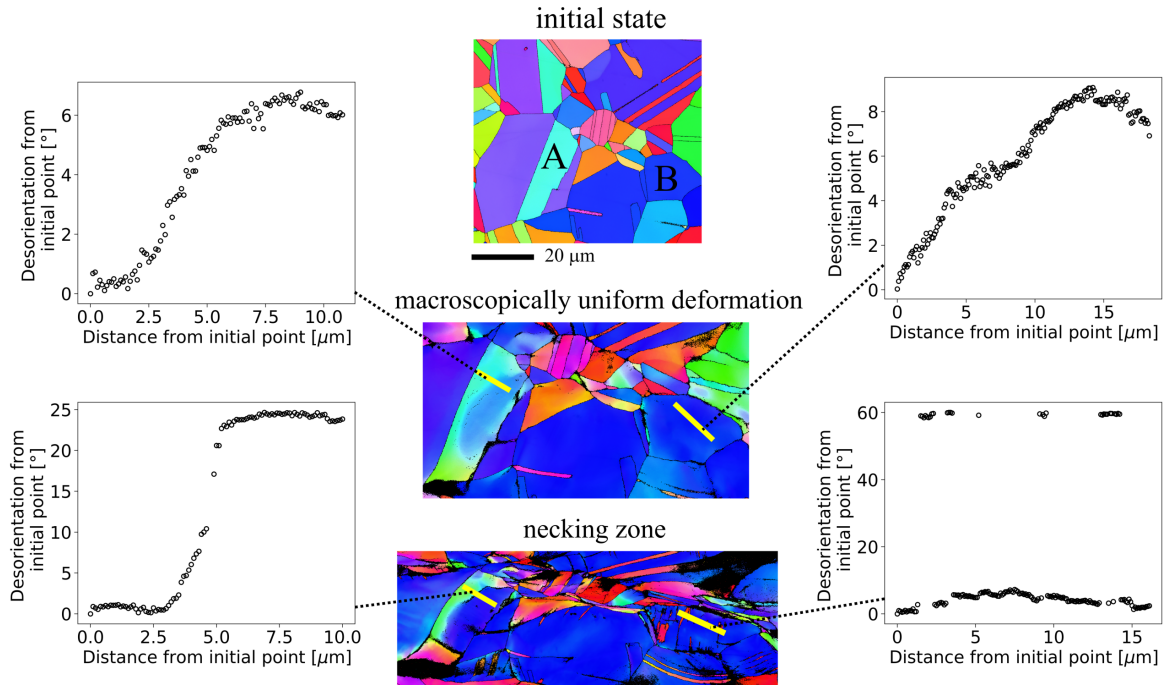


Figure 8: Disorientation profiles in grains A and B at different deformation stages.

In the macroscopically uniform regime, both grains deform predominantly by dislocation slip, with orientation changes of approximately  $7^\circ$  (grain A) and  $9^\circ$  (grain B). The observed gradients indicate a significant contribution of geometrically necessary dislocations (GNDs) to strain accommodation. During localized deformation, grain A continues to deform primarily by slip, with orientation changes increasing to  $35^\circ$ , leading to sub-boundary formation and fragmentation into subgrains. In contrast, grain B exhibits behaviour consistent with deformation twinning, preceded by slip activity. The formation of twins results in a lamellar twin-matrix structure and pronounced grain subdivision.

As described in Section 2, the second experimental approach involved EBSD mapping of regions corresponding to known strain levels, enabling analysis of microtexture evolution. Measurements performed at different through-thickness locations showed consistent crystallographic orientation distributions, and mid-thickness maps were therefore selected as representative. Figure 9 presents orientation maps together with (111) and (100) pole figures for strain levels of 0, 0.2, 0.3, 0.35, and 0.45 (just prior to fracture). The corresponding orientation distribution functions (ODFs) are shown in the  $\phi_2 = 45^\circ$  section. The texture was calculated using OIM Analysis software based on a harmonic series expansion method with a series rank of 22. The texture is represented using Euler angles in the Bunge convention, and the ODF sections were computed with an angular resolution of  $1^\circ$  in both  $\phi_1$  and  $\Phi$ .

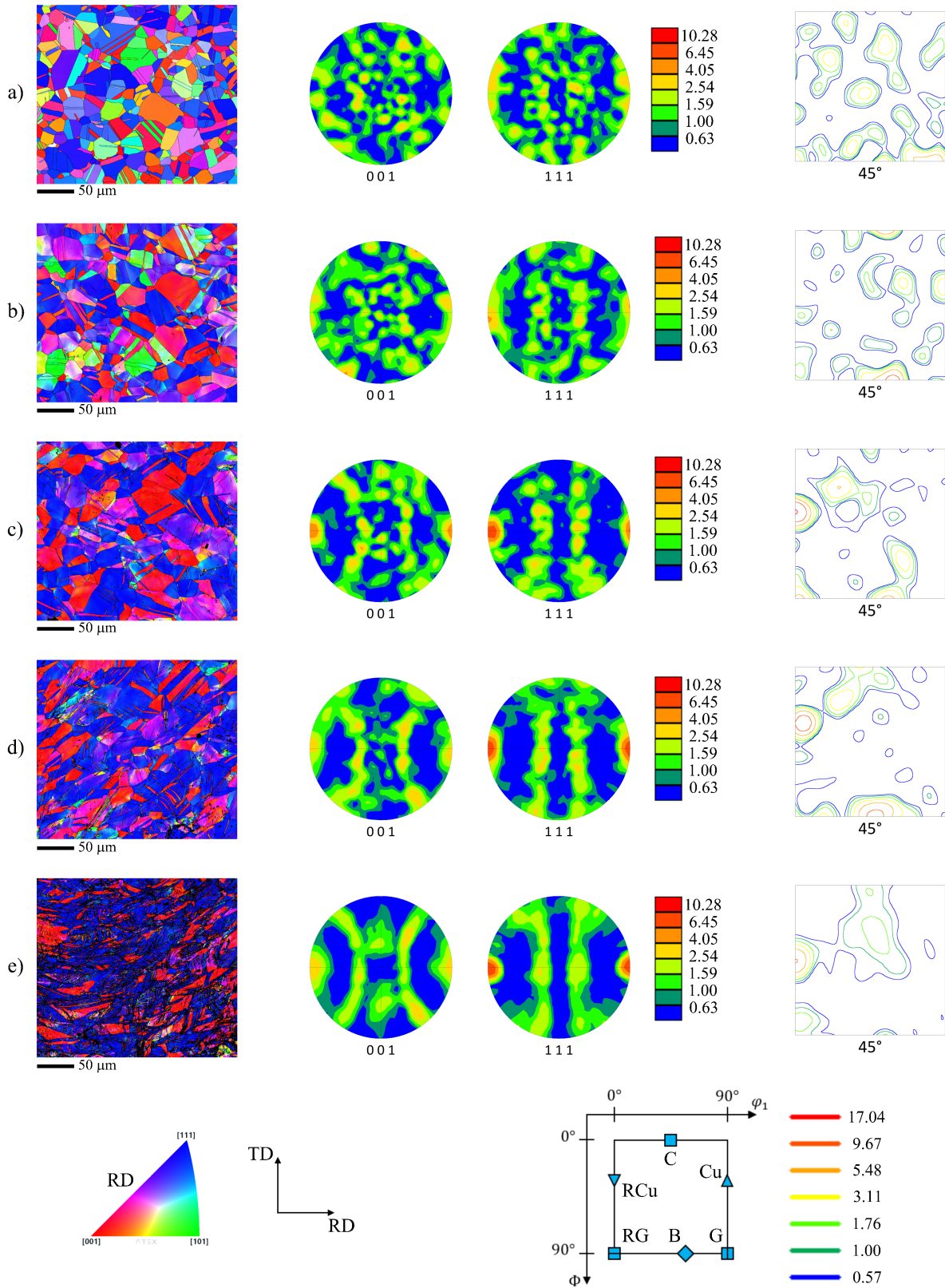


Figure 9: Orientation maps with respect to the tensile direction, the corresponding (111) and (100) pole figures and ODFs in the  $\phi_2 = 45^\circ$  section for the successive values of the equivalent plastic strain: (a) 0 (initial state), (b) 0.2, (c) 0.3, (d) 0.35, and (e) 0.45 (just before fracture).

In the initial state, the material exhibits a weak crystallographic texture inherited from rolling and subsequent heat treatment (Fig. 9a). At  $\bar{\varepsilon}^p = 0.2$ , the texture remains relatively weak (Fig. 9b), although the Goss component (G,  $\{110\}\langle 100\rangle$ ), located near  $\phi_1 = 90^\circ$ ,  $\Phi = 90^\circ$ ,  $\phi_2 = 45^\circ$ , diminishes and intensity develops near the Brass component (B,  $\{110\}\langle 112\rangle$ ), located at  $\phi_1 = 55^\circ$ ,  $\Phi = 90^\circ$ ,  $\phi_2 = 45^\circ$ .

For equivalent plastic strain between 0.2 and 0.3, deformation-induced components become more distinct and a redistribution of orientations occurs. The texture is dominated by Brass, Rotated Copper (RCu,  $\{112\}\langle 110\rangle$ ), and Rotated Goss (RG,  $\{110\}\langle 110\rangle$ ) components. Simultaneously, the Copper (C,  $\{112\}\langle 111\rangle$ ) and Goss (G) components progressively vanish, indicating their instability under continued tensile loading. Grain rotations align  $\langle 111\rangle$  and  $\langle 100\rangle$  directions with the tensile axis, leading to the development of a dual-fibre texture, with the  $\langle 111\rangle \parallel$  RD fibre being dominant, consistent with the medium SFE of 310S steel [37]. Similar dual-fibre evolution has been reported in another TWIP steels [38, 39]. At  $\bar{\varepsilon}^p \approx 0.3$ , the Brass component spreads toward the Rotated Copper orientation through a continuous lattice rotation of approximately  $30^\circ$  about a  $\langle 111\rangle$  axis. This behaviour is consistent with crystallographic slip on  $\{111\}\langle 110\rangle$  systems under relatively homogeneous deformation conditions.

A qualitative transition occurs between  $\bar{\varepsilon}^p = 0.35$  and  $\bar{\varepsilon}^p = 0.45$ . At  $\bar{\varepsilon}^p = 0.35$ , the texture remains relatively compact and aligned with the  $\langle 111\rangle \parallel$  RD fibre, indicating that deformation is still governed by planar slip and twinning-assisted rotation. In contrast, at  $\bar{\varepsilon}^p = 0.45$  (necking regime), the Brass component becomes diffuse, reflecting orientation fragmentation associated with strong local lattice curvature and grain subdivision. The increased intensity near the Rotated Goss component indicates a partial transition toward the  $\langle 100\rangle \parallel$  RD fibre. Such redistribution cannot be explained by homogeneous slip alone and points to the activation of localized shear mechanisms. The observed transition  $B \rightarrow (RCu + RG)$  is therefore consistent with shear-band-mediated lattice rotation, as reported for FCC materials undergoing large strain deformation [40].

The evolution of deformation mechanisms was further quantified through analysis of  $\Sigma 3$  twin boundaries (Fig. 10).

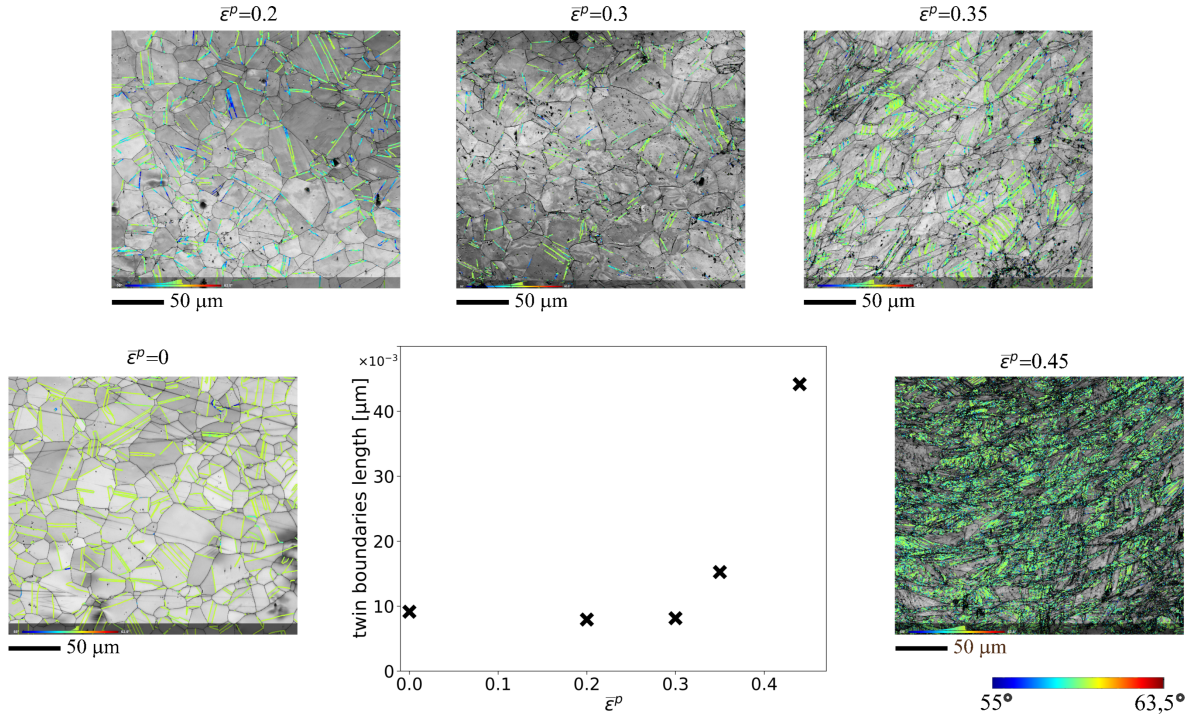


Figure 10: IQ maps for the analysed strain levels, with marked CSL  $\Sigma 3 - 60^\circ \langle 111 \rangle$  twin boundaries, and a plot showing the relationship between total twin boundary length and equivalent plastic strain.

In the reference state, only annealing twins are present. Up to  $\bar{\epsilon}^P = 0.3$ , the total twin boundary length remains nearly constant, indicating that deformation is primarily accommodated by dislocation slip. Beyond this strain, a rapid increase in twin boundary length is observed, corresponding to the onset of deformation twinning within the resolution limits of EBSD. At  $\bar{\epsilon}^P = 0.35$ , numerous deformation twins form, predominantly in grains with  $\langle 111 \rangle \parallel \text{RD}$  orientation, resulting in a fine lamellar twin–matrix structure. At  $\bar{\epsilon}^P = 0.45$ , this lamellar morphology becomes pervasive. Twinning does not introduce new texture components but redistributes the existing orientations: twins formed in  $\langle 111 \rangle \parallel \text{RD}$  grains promote the development of the  $\langle 100 \rangle \parallel \text{RD}$  fibre.

High-resolution EBSD maps (Fig. 11) reveal a progressive increase in twin density and thickness with increasing strain. Moreover, deformation twins are not randomly distributed but form in crystallographically related variants that interact with one another. These variants are commonly organized into twin packets, in which multiple twin systems sharing a common  $\{111\}$  habit plane operate within a single grain, leading to mutual impingement and progressive subdivision of the matrix into finer domains.

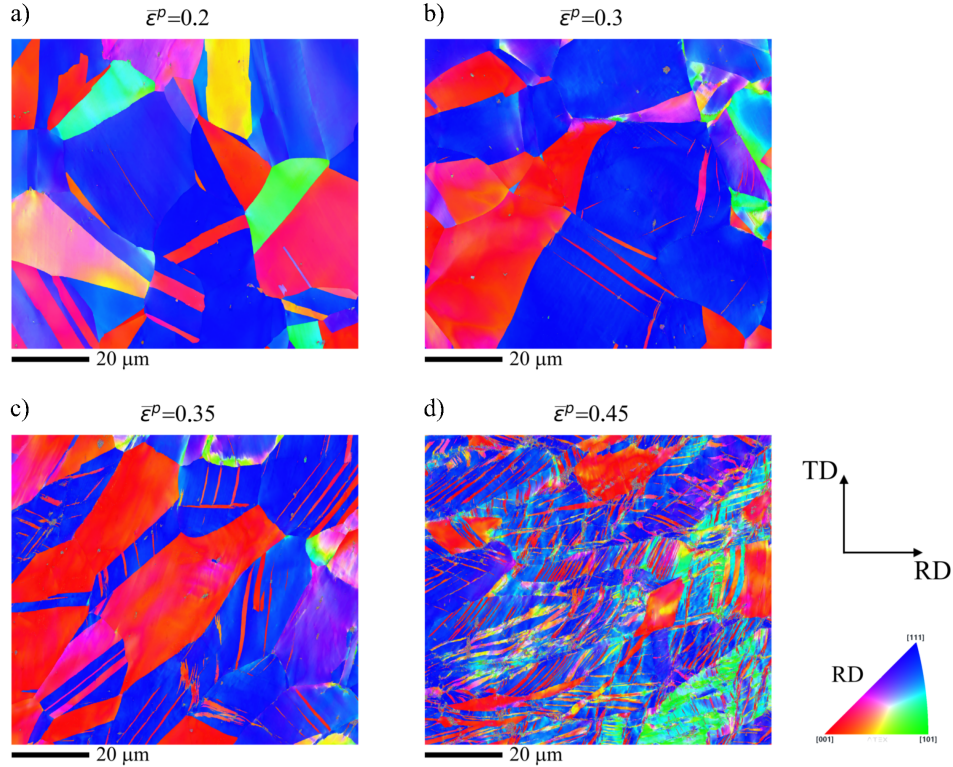


Figure 11: Orientation maps relative to the tensile direction, acquired at 3000x magnification with a 50 nm step size, for increasing equivalent plastic strain levels of (a) 0.2, (b) 0.3, (c) 0.35, and (d) 0.45 (just before specimen fracture).

The resulting lamellar structure markedly reduces the dislocation mean free path – consistent with twinning-induced hardening (dynamic Hall–Petch effect) in TWIP steels [41, 42] – and also enhances strain partitioning while promoting activation of multiple slip systems. These effects increase local strain incompatibility, thereby facilitating the development of localized deformation modes.

Figure 12 presents EBSD results obtained from the ND–RD section (longitudinal cross-section) in the necking zone, just prior to fracture. Overview and high-resolution maps are shown to highlight both the global morphology and local deformation features. Figure 12a shows an IPF map (aligned with RD) acquired at lower magnification (1500x kx, step size 200 nm). A representative subarea, outlined by a black dashed contour, is examined in greater detail in Fig. 12b and c, which were acquired at higher magnification (3500 kx) with a refined step size of 50 nm. Figure 12b presents the corresponding IPF map (aligned with RD), while Fig. 12c shows the Kernel Average Mismatch (KAM) map.

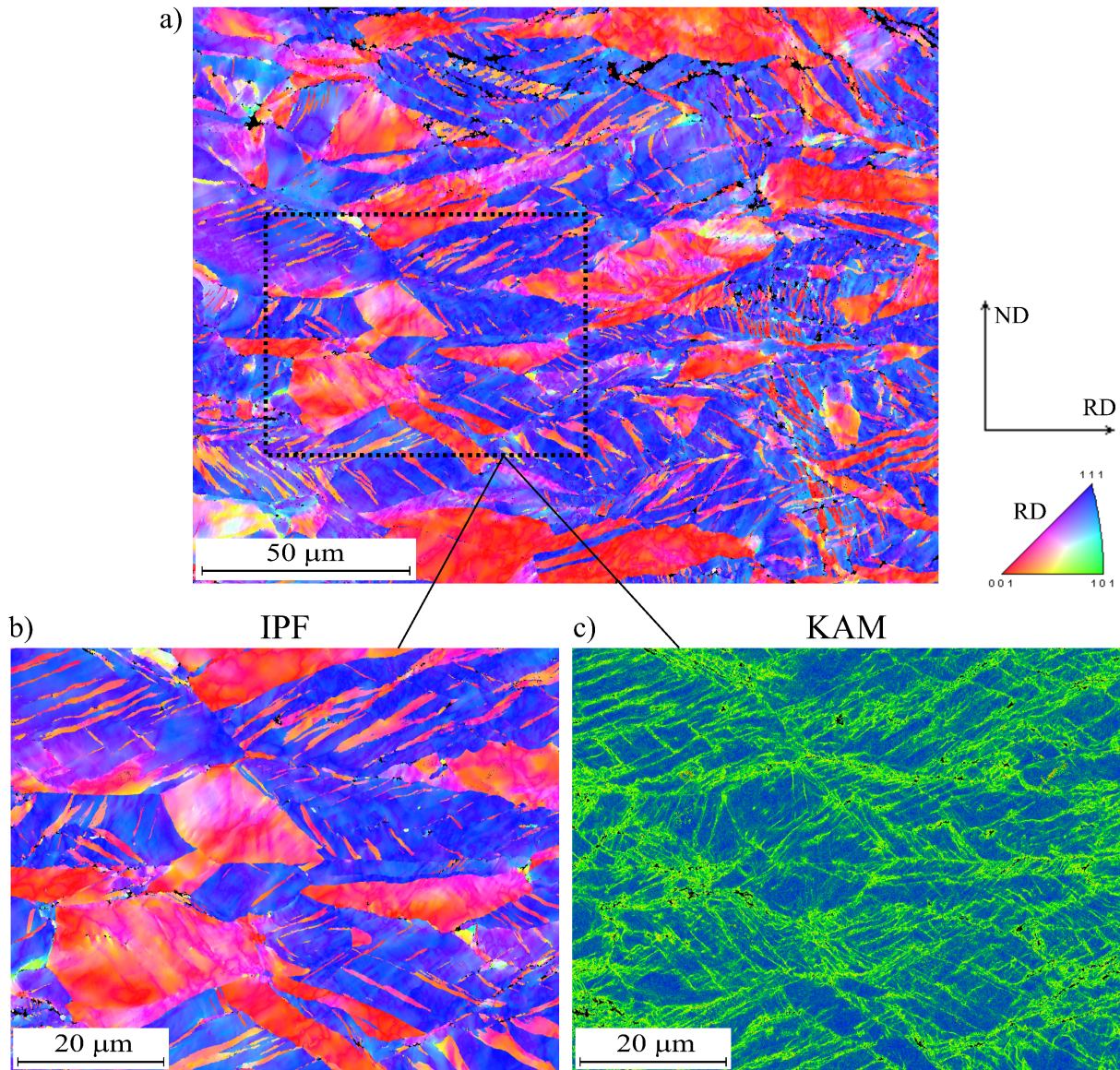


Figure 12: EBSD maps from the ND–RD section (longitudinal cross-section) in the necking zone obtained just prior to fracture: (a) overview IPF map (aligned with RD) acquired at 1500x with a 200 nm step size, (b) high-resolution IPF map (aligned with RD) of the subarea marked in (a), acquired at 3500x with a 50 nm step size, (c) corresponding Kernel Average Misorientation (KAM) map.

The IPF maps reveal a pronounced longitudinal morphology characterized by a well-developed lamellar twin–matrix structure. Regions with  $\langle 111 \rangle \parallel$  RD orientations (associated with B and RCu components) coexist with  $\langle 100 \rangle \parallel$  RD regions (associated with the RG component and deformation twins), indicating significant orientation redistribution during deformation. The KAM map exhibits elevated local misorientation concentrated within twin-related domains, forming partially continuous high-strain channels aligned close to  $\{111\}$  traces, consistent with incipient shear localization. These channel-like features appear quasi-parallel due to

geometrical constraints imposed by the lamellar structure and are inclined at approximately  $20\text{--}45^\circ$  to the tensile axis, consistent with shear-band angles reported in the literature [43, 40]. Within this framework, deformation twinning plays an indirect but critical role: rather than directly forming new texture components, it refines the microstructure and promotes strain heterogeneity, thus facilitating shear-band formation.

The microstructural evolution described above has a direct impact on macroscopic energy storage. Figure 13 compares the evolution of the energy storage rate  $Z$  with the total twin boundary length. At low strains,  $Z$  decreases rapidly while the twin boundary length remains nearly constant, indicating that energy storage is controlled by dislocation structure evolution. According to the LEDS theory [32], this decrease reflects the formation of progressively lower-energy dislocation configurations.

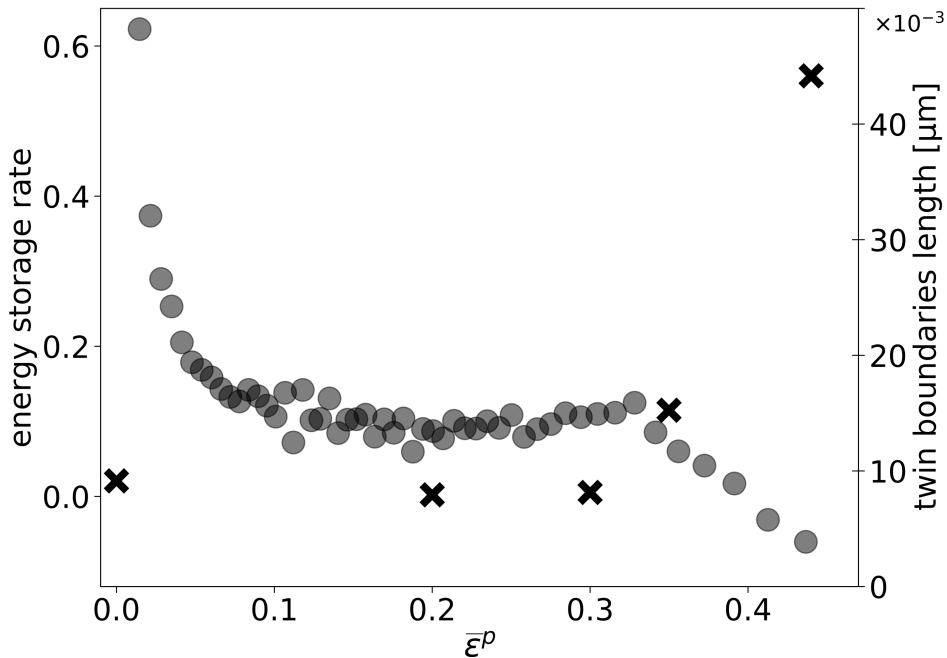


Figure 13: Variation in total twin boundary length ( $\times$ ) and energy storage rate ( $\cdot$ ) as a function of equivalent plastic strain  $\bar{\epsilon}^p$

In the strain range  $0.15 \leq \bar{\epsilon}^p \leq 0.3$ , both  $Z$  and twin boundary length remain relatively stable, consistent with homogeneous deformation dominated by dislocation slip. A clear transition occurs beyond  $\bar{\epsilon}^p \approx 0.3$ : the rapid increase in twin boundary length is accompanied by a continued decrease in  $Z$ . This indicates that, although twinning introduces additional interfaces capable of storing energy, it concurrently promotes strain localization and, indirectly - through refinement of the lamellar structure - enhances energy dissipation.

In the necking regime, the microstructure is highly heterogeneous, comprising twin-free regions exhibiting strong orientation gradients and regions dominated by a fine lamellar twin-matrix structure (Fig. 12a,b), which, on the macroscopic scale, coincides with the area where  $Z$  becomes non-positive (Fig. 4a). This behaviour is consistent with earlier observations in austenitic steels, where strain localization and shear banding were associated with a loss of energy storage capacity [31]. Numerous studies have shown that layered microstructures composed of twins or dislocation arrangements promote shear band propagation [44, 45, 46]. Within such bands, intense plastic deformation may activate recovery or dynamic recrystallization processes [47], providing a mechanism for the local release of stored energy.

## 4. Summary and conclusions

A microstructural interpretation of energy storage during plastic deformation of 310S TWIP steel was developed by correlating EBSD-based characterization of crystallographic orientation evolution with previously determined macroscopic energy conversion data. The analysis focused in particular on the stage of strain localization.

The main conclusions are as follows:

- (i) Plastic deformation proceeds through a transition from dislocation-slip-dominated behaviour at low strains to a regime of pronounced twinning activity beyond  $\bar{\epsilon}^p \approx 0.3$ . This transition governs both grain-scale lattice rotation and the development of internal orientation gradients.
- (ii) Progressive deformation leads to the formation of a dual-fibre texture with dominant  $\langle 111 \rangle \parallel \text{RD}$  and secondary  $\langle 100 \rangle \parallel \text{RD}$  components. At advanced stages, texture evolution departs from homogeneous rotation paths and reflects increasing deformation heterogeneity.
- (iii) Deformation twinning does not introduce new texture components directly but refines the microstructure into a lamellar twin-matrix morphology. This refinement promotes strain partitioning, enhances local lattice curvature, and facilitates further crystallographic rotation under non-uniform deformation conditions.
- (iv) In the necking regime, the observed redistribution of texture components ( $\text{B} \rightarrow \text{RCu/RG}$ ) and the development of orientation fragmentation are consistent with shear-dominated deformation. The evolved lamellar structure and associated strain heterogeneities provide favourable conditions for shear bands initiation and propagation.

(v) The evolution of microstructure is directly reflected in the macroscopic energy storage behaviour. The initial decrease in the energy storage rate  $Z$  is associated with dislocation rearrangement processes, while the onset of twinning does not lead to an increase in stored energy. Instead, during strain localization, the formation of a highly refined twin–matrix structure and intensified lattice rotations coincide with a reduction of  $Z$  to zero or negative values.

These findings demonstrate that energy storage in TWIP steels cannot be interpreted solely in terms of defect density. Instead, crystallographic reorientation, twinning-induced microstructural refinement, and strain localization collectively govern the transition toward deformation mechanisms that limit further energy storage and promote dissipation. The proposed approach provides a new microstructural perspective for interpreting energy conversion in FCC materials where deformation twinning plays a dominant role.

## Data availability

The data supporting the findings of this study are available on Zenodo at <https://doi.org/10.5281/zenodo.18878199>.

## Declaration of competing interest

The authors declare that they have no known competing financial interests or personal relationships that could have appeared to influence the work reported in this paper.

## Acknowledgements

The authors thank Leszek Urbański for performing the EBSD sample preparation, essential for the microstructural characterization presented in this work.

## References

- [1] L. Remy, A. Pineau, Twinning and strain-induced f.c.c.  $\rightarrow$  h.c.p. transformation in the femnrc system, *Materials Science and Engineering* 28 (1) (1977) 99–107. doi: 10.1016/0025-5416(77)90093-3.

- [2] C. Ullrich, R. Eckner, L. Krüger, S. Martin, V. Klemm, D. Rafaja, Interplay of microstructure defects in austenitic steel with medium stacking fault energy, *Materials Science and Engineering: A* 649 (2016) 390–399. doi:10.1016/j.msea.2015.10.021.
- [3] I. Karaman, H. Sehitoglu, K. Gall, Y. I. Chumlyakov, H. J. Maier, Deformation of single crystal hadfield steel by twinning and slip, *Acta Materialia* 48 (6) (2000) 1345–1359. doi:10.1016/S1359-6454(99)00383-3.
- [4] P. Yang, Q. Xie, L. Meng, H. Ding, Z. Tang, Dependence of deformation twinning on grain orientation in a high manganese steel, *Scripta Materialia* 55 (7) (2006) 629–631. doi:10.1016/j.scriptamat.2006.06.004.
- [5] T. T. Huang, W. J. Dan, W. G. Zhang, Study on the strain hardening behaviors of twip/trip steels, *Metallurgical and Materials Transactions A* 48 (2017) 4553—4564. doi:10.1007/s11661-017-4245-0.
- [6] P. J. Brofman, G. S. Ansell, On the effect of carbon on the stacking fault energy of austenitic stainless steels, *Metallurgical Transactions A* 9 (6) (1978) 879–880. doi:doi.org/10.1007/BF02649799.
- [7] K. Chen, L. Zhang, Z. Shen, X. Zeng, Revealing the oxidation mechanism of 310s stainless steel in supercritical water via high-resolution characterization, *Corrosion Science* 200 (2022) 110212. doi:10.1016/j.corsci.2022.110212.
- [8] A. Grajcar, A. Kozłowska, S. Topolska, M. Morawiec, Effect of deformation temperature on microstructure evolution and mechanical properties of low-carbon high-mn steel, *Advances in Materials Science and Engineering* 2018 (1) (2018) 7369827. doi:10.1155/2018/7369827.
- [9] S. Lee, Y. Estrin, B. C. De Cooman, Effect of the strain rate on the trip–twip transition in austenitic fe-12 pct mn-0.6 pct c twip steel, *Metallurgical and materials transactions A* 45 (2) (2014) 717–730. doi:10.1007/s11661-013-2028-9.
- [10] I. Gutierrez-Urrutia, S. Zaeferrer, D. Raabe, The effect of grain size and grain orientation on deformation twinning in a fe–22wt.% mn–0.6wt.% c twip steel, *Materials Science and Engineering: A* 527 (15) (2010) 3552–3560. doi:10.1016/j.msea.2010.02.041.
- [11] K. M. Rahman, V. A. Vorontsov, D. Dye, The effect of grain size on the twin initiation stress in a twip steel, *Acta Materialia* 89 (2015) 247–257. doi:10.1016/j.actamat.2015.02.008.

- [12] D. M. Field, D. J. Magagnosc, B. Hornbuckle, J. T. Lloyd, K. R. Limmer, Manipulation of the stacking fault energy of a medium-mn steel through temperature and hierarchical compositional variation, *Metallurgical and Materials Transactions A* 55 (2024) 161—172. doi:10.1007/s11661-023-07239-x.
- [13] X. Wang, R. R. D. Vecchis, C. Li, H. Zhang, X. Hu, S. Sridar, Y. Wang, W. Chen, W. Xiong, Design metastability in high-entropy alloys by tailoring unstable fault energies, *Science Advances* 8 (36) (2022) eabo7333. doi:10.1126/sciadv.abo7333.
- [14] H. Yan, X. Zhao, Y. Z. N. Jia, T. He, Influence of shear banding on the formation of brass-type textures in polycrystalline fcc metals with low stacking fault energy, *Journal of Materials Sciences and Technology* 30 (4) (2014) 408–416. doi:10.1016/j.jmst.2013.11.010.
- [15] E. El-Danaf, S. R. Kalidindi, R. D. Doherty, C. Necker, Deformation texture transition in brass: critical role of micro-scale shear bands, *Acta Materialia* 48 (10) (2000) 2665–2673. doi:10.1016/S1359-6454(00)00050-1.
- [16] H. Paul, J. H. Driver, C. Maurice, A. Piątkowski, The role of shear banding on deformation texture in low stacking fault energy metals as characterized on model Ag crystals, *Acta Materialia* 55 (2) (2007) 575–588. doi:10.1016/j.actamat.2006.08.051.
- [17] A. L. Titchener, M. B. Bever, The stored energy of cold work, *Progress in Metal Physics* 7 (1958) 247–338. doi:10.1016/0079-6425(73)90001-7.
- [18] G. I. Taylor, H. Quinney, The latent energy remaining in a metal after cold working, *Proceedings of the Royal Society of London. Series A, Containing Papers of a Mathematical and Physical Character* 143 (849) (1934) 307–326. doi:DOI:10.1098/rspa.1934.0004.
- [19] A. Wolfenden, The energy stored in polycrystalline copper deformed at room temperature, *Acta Metallurgica* 19 (12) (1971) 1373–1377. doi:10.1016/0001-6160(71)90075-7.
- [20] A. Chrysochoos, O. Maisonneuve, G. Martin, H. Caumon, J. C. Chezeaux, Plastic and dissipated work and stored energy, *Nuclear Engineering and Design* 114 (3) (1989) 323–333. doi:10.1016/0029-5493(89)90110-6.
- [21] W. Oliferuk, W. A. Świątnicki, M. W. Grabski, Effect of the grain size on the rate of energy storage during the tensile deformation of an austenitic steel, *Materials Science and Engineering: A* 197 (1) (1995) 49–58. doi:10.1016/0921-5093(94)09766-6.

- [22] W. Oliferuk, M. Maj, Stress–strain curve and stored energy during uniaxial deformation of polycrystals, *European Journal of Mechanics-A/Solids* 28 (2) (2009) 266–272. doi:10.1016/j.euromechsol.2008.06.003.
- [23] W. Oliferuk, S. P. Gadaj, M. W. Grabski, Energy storage during the tensile deformation of armco iron and austenitic steel, *Materials Science and Engineering: A* 70 (1985) 131–141. doi:10.1016/0025-5416(85)90274-5.
- [24] L. Li, J. M. Muracciole, L. Waltz, L. Sabatier, F. Barou, B. Wattrisse, Local experimental investigations of the thermomechanical behavior of a coarse-grained aluminum multicrystal using combined dic and irt methods, *Optics and Lasers in Engineering* 81 (2016) 1–10. doi:10.1016/j.optlaseng.2016.01.001.
- [25] H. Louche, A. Chrysochoos, Thermal and dissipative effects accompanying lüders band propagation, *Materials Science and Engineering: A* 307 (1-2) (2001) 15–22. doi:10.1016/S0921-5093(00)01975-4.
- [26] X. G. Wang, L. Wang, M. X. Huang, Kinematic and thermal characteristics of lüders and portevin-le châtelier bands in a medium mn transformation-induced plasticity steel, *Acta Materialia* 124 (2017) 17–29. doi:10.1016/j.actamat.2016.10.069.
- [27] L. Bodelot, L. Sabatier, E. Charkaluk, P. Dufrénoy, Experimental setup for fully coupled kinematic and thermal measurements at the microstructure scale of an aisi 316l steel, *Materials Science and Engineering: A* 501 (1-2) (2009) 52–60. doi:10.1016/j.msea.2008.09.053.
- [28] A. Chrysochoos, B. Wattrisse, J.-M. Muracciole, Y. El Kaïm, Fields of stored energy associated with localized necking of steel, *Journal of Mechanics of Materials and Structures* 4 (2) (2009) 245–262. doi:10.2140/jomms.2009.4.241.
- [29] P. Knysh, Y. P. Korkolis, Determination of the fraction of plastic work converted into heat in metals, *Mechanics of Materials* 86 (2015) 71–80. doi:10.1016/j.mechmat.2015.03.006.
- [30] S. Musiał, M. Maj, L. Urbański, M. Nowak, Field analysis of energy conversion during plastic deformation of 310s stainless steel, *International Journal of Solids and Structures* (2022) 111411doi:10.1016/j.ijsolstr.2021.111411.
- [31] W. Oliferuk, M. Maj, Plastic instability criterion based on energy conversion, *Materials Science and Engineering: A* 462 (1-2) (2007) 363–366. doi:10.1016/j.msea.2006.02.465.

- [32] N. Hansen, D. Kuhlmann-Wilsdorf, Low energy dislocation structures due to unidirectional deformation at low temperatures, *Materials Science and Engineering: A* 81 (1986) 141–161. doi:10.1016/0025-5416(86)90258-2.
- [33] D. Kuhlmann-Wilsdorf, Leds: Properties and effects of low energy dislocation structures, *Materials Science and Engineering: A* 86 (1987) 53–66. doi:10.1016/0025-5416(87)90442-3).
- [34] D. Kuhlmann-Wilsdorf, Q: Dislocations structures—how far from equilibrium? a: Very close indeed, *Materials Science and Engineering: A* 315 (1-2) (2001) 211–216. doi:10.1016/S0921-5093(01)01204-7.
- [35] B. Beausir, J. J. Fundenberger, Analysis tools for electron and x-ray diffraction, ATEX-software, www.atex-software.eu, Université de Lorraine-Metz (2017).
- [36] S. Godet, L. Jiang, A. A. Luo, J. J. Jonas, Use of schmid factors to select extension twin variants in extruded magnesium alloy tubes, *Scripta Materialia* 55 (11) (2006) 1055–1058. doi:10.1016/j.scriptamat.2006.07.059.
- [37] I. L. Dillamore, The stacking fault energy dependence of the mechanisms of deformation in fcc metals, *Metallurgical Transactions* 1 (1970) 2463–2470. doi:10.1007/BF03038371.
- [38] B. C. De Cooman, Y. Estrin, S. K. Kim, Twinning-induced plasticity (twip) steels, *Acta Materialia* 142 (2018) 283–362. doi:10.1016/j.actamat.2017.06.046.
- [39] D. Barbier, N. Gey, S. Allain, N. Bozzolo, M. Humbert, Analysis of the tensile behavior of a twip steel based on the texture and microstructure evolutions, *Materials Science and Engineering: A* 500 (1-2) (2009) 196–206. doi:10.1016/j.msea.2008.09.031.
- [40] H. Paul, J. H. Driver, C. Maurice, Z. Jasiński, Shear band microtexture formation in twinned face centred cubic single crystals, *Materials Science and Engineering: A* 359 (1-2) (2003) 178–191. doi:10.1016/S0921-5093(03)00335-6.
- [41] K. Yao, X. Min, Static and dynamic hall–petch relations in  $\{332\}\langle 113 \rangle$  twip ti–15mo alloy, *Materials Science and Engineering: A* 827 (2021) 142044. doi:10.1016/j.msea.2021.142044.
- [42] G. Frommeyer, U. Brück, P. Neumann, Supra-ductile and high-strength manganese-trip/twip steels for high energy absorption purposes, *ISIJ international* 43 (3) (2003) 438–446. doi:10.2355/isijinternational.43.438.

- [43] W. Y. Yeung, B. J. Duggan, Shear band angles in rolled fcc materials, *Acta Metallurgica* 35 (2) (1987) 541–548. doi:10.1016/0001-6160(87)90259-8.
- [44] B. J. Duggan, M. Hatherly, W. B. Hutchinson, P. T. Wakefield, Deformation structures and textures in cold-rolled 70: 30 brass, *Metal Science* 12 (8) (1978) 343–351. doi:10.1179/030634578790433909.
- [45] K. Morii, H. Mecking, Y. Nakayama, Development of shear bands in fcc single crystals, *Acta Metallurgica* 33 (3) (1985) 379–386. doi:10.1016/0001-6160(85)90080-X.
- [46] T. Leffers, J. B. Bilde-Sørensen, Intra-and intergranular heterogeneities in the plastic deformation of brass during rolling, *Acta Metallurgica et Materialia* 38 (10) (1990) 1917–1926. doi:10.1016/0956-7151(90)90303-X.
- [47] M. A. Meyers, G. Subhash, B. K. Kad, L. Prasad, Evolution of microstructure and shear-band formation in  $\alpha$ -hcp titanium, *Mechanics of Materials* 17 (2-3) (1994) 175–193. doi:10.1016/0167-6636(94)90058-2.